

See discussions, stats, and author profiles for this publication at: <https://www.researchgate.net/publication/256847957>

Adsorption and Decomposition of Formic Acid on Model Ceria and Pt/Ceria Catalysts

ARTICLE *in* THE JOURNAL OF PHYSICAL CHEMISTRY C · JUNE 2013

Impact Factor: 4.77 · DOI: 10.1021/Jp311008v

CITATIONS

12

READS

76

10 AUTHORS, INCLUDING:



[Yaroslava Lykhach](#)

Friedrich-Alexander-University of Erlangen-Nü...

38 PUBLICATIONS 620 CITATIONS

[SEE PROFILE](#)



[Markus Happel](#)

Friedrich-Alexander-University of Erlangen-Nü...

24 PUBLICATIONS 424 CITATIONS

[SEE PROFILE](#)



[Nataliya Tsud](#)

Charles University in Prague

107 PUBLICATIONS 1,042 CITATIONS

[SEE PROFILE](#)



[Kevin Charles Prince](#)

Sincrotrone Trieste S.C.p.A.

479 PUBLICATIONS 7,080 CITATIONS

[SEE PROFILE](#)

Adsorption and Decomposition of Formic Acid on Model Ceria and Pt/Ceria Catalysts

Yaroslava Lykhach,^{*,†} Markus Happel,[†] Viktor Johánek,[‡] Tomáš Skála,[‡] Fabian Kollhoff,[†] Nataliya Tsud,[‡] Filip Dvořák,[‡] Kevin C. Prince,^{§,||} Vladimír Matolín,[‡] and Jörg Libuda^{†,⊥}

[†]Lehrstuhl für Physikalische Chemie II, Friedrich-Alexander-Universität Erlangen-Nürnberg, Egerlandstrasse 3, 91058 Erlangen, Germany

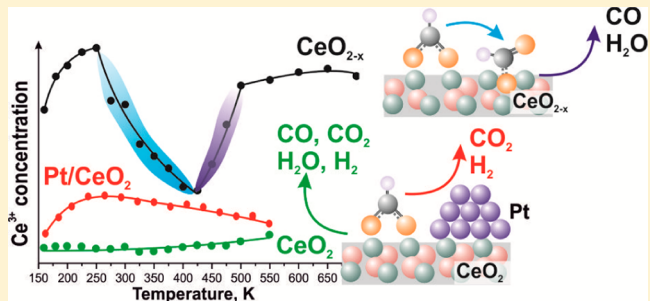
[‡]Department of Surface and Plasma Science, Faculty of Mathematics and Physics, Charles University, V Holešovičkách 2, 18000 Prague, Czech Republic

[§]Sincrotrone Trieste SCpA, Strada Statale 14, km 163.5, 34149 Basovizza-Trieste, Italy

^{||}IOM, Strada Statale 14, km 163.5, 34149 Basovizza-Trieste, Italy

[⊥]Erlangen Catalysis Resource Center, Friedrich-Alexander-Universität Erlangen-Nürnberg, Egerlandstrasse 3, 91058 Erlangen, Germany

ABSTRACT: Adsorption and reaction of formic acid on stoichiometric $\text{CeO}_2(111)$, partially reduced CeO_{2-x} , and Pt/ $\text{CeO}_2(111)$ films prepared on Cu(111) were studied by means of synchrotron radiation photoelectron spectroscopy (SRPES), resonant photoemission spectroscopy (RPES), infrared reflection absorption spectroscopy (IRAS), and temperature-programmed desorption (TPD). On all studied samples, the principal species formed during formic acid adsorption below 160 K were formate and molecular formic acid. In the presence of Pt particles, formate species were predominantly localized on Pt at 100 K, and on ceria at or above 300 K. Below 400 K, molecular formic acid decomposes to formate with partial release of CO_2 , CO, hydrogen, and water. Analysis of the TPD fragmentation suggests additional evolution of methane. Above 400 K, desorption of CO_2 , CO, hydrogen, and water is observed. This process is controlled by the stoichiometry of ceria and the presence of Pt particles. In particular, desorption of CO_2 is suppressed on CeO_{2-x} but is enhanced on Pt/ CeO_2 . RPES suggests that the reaction of formic acid does not alter the oxidation state of cerium cations on $\text{CeO}_2(111)$. By contrast, we observed significant reoxidation on partially reduced CeO_{2-x} between 250 and 400 K, followed by reduction between 400 and 500 K.



1. INTRODUCTION

Bioderived hydrocarbons draw increasing attention as a potential feedstock for hydrogen production.¹ One potential route involves conversion of biomass by flash pyrolysis into a bio-oil, a liquid mixture of aliphatic and aromatic hydrocarbon oxygenates containing aldehydes, acids, alcohols, ketones, and so on. The subsequent conversion of the bio-oil via steam reforming is generally hindered by rapid catalyst deactivation due to coke deposition.² The exact mechanisms of this deactivation process are yet unknown. The detailed understanding of the related surface chemistry and identification of the structure–activity correlations requires fundamental studies of model oxygenate compounds on well-defined catalyst surfaces.

As a very simple model compound, we study formic acid (HCOOH). On many metallic^{3–10} surfaces, formic acid dissociates to produce formate (HCOO) and hydrogen (H). On oxides,^{11–19} deprotonation of formic acid through the loss of acidic H^+ yields formate (HCOO^-) and hydroxyl (OH^-). The formate decomposes either via dehydrogenation or

dehydration pathways, yielding desorption of CO_2/H_2 , or $\text{CO}/\text{H}_2\text{O}$, respectively. It was found that dehydrogenation is the dominant pathway on metals whereas dehydration prevails on oxides.^{7,8} Furthermore, dehydration is favored on acidic oxides while dehydrogenation occurs on basic oxides.²⁰ On the surfaces where only one set of desorption products occurs, i.e. either CO_2/H_2 or $\text{CO}/\text{H}_2\text{O}$, the reaction proceeds via a simple monomolecular decomposition. On the surfaces where both sets are formed, the reaction may proceed via a bimolecular mechanism that involves interaction between two formates or a formate and a formic acid. The bimolecular mechanism was also suggested to be predominant under steady state conditions; in this case decomposition of surface formate is accelerated by interaction with gaseous formic acid.⁶ Bandara et al.^{20,21} reported substantial differences between decomposition of formic acid under steady state and ultrahigh vacuum (UHV)

Received: November 7, 2012

Revised: May 10, 2013

Published: May 21, 2013

conditions. The authors reported that the reaction temperature is an important parameter for selectivity. On oxides, selectivity can be modified by the creation of vacancies.^{13–16}

Under UHV conditions, the bonding configuration of the surface formate may promote a particular decomposition pathway.^{22,23} On metal and oxide surfaces, different bonding geometries such as monodentate, bidentate chelating, and bridging formates have been identified.^{3,7,9–11,17–19,24,25} For unimolecular mechanisms, Borowiak et al.²² predicted that formate adsorbed on oxide surfaces in monodentate and bridging configurations favors dehydration, while bidentate formate prefers the dehydrogenation pathway. The authors emphasized the relation between the OCO bending and asymmetric stretching modes and the selectivity of the reaction. This argument, however, does not hold for the bimolecular mechanism.²³ For instance, on Ni(110) bimolecular dehydration produces an intermediate, formic anhydride, that decomposes to CO₂/H₂ and CO/H₂O with a fixed CO₂/CO ratio of 1.^{26,27}

Adsorption and decomposition of formic acid has been studied on various oxides: CeO₂,^{15,24,28} TiO₂,^{29,30} SnO₂,¹³ UO₂,¹⁴ NiO,^{20,21,31–33} and so on, as well as on metals: Pt,^{7,34–36} Pd,³⁴ Ni,³⁴ Rh,³⁷ Cu,^{6,38,39} and so on. Since the current paper is concerned with the formic acid reactions on Pt/CeO₂ catalysts, we briefly reiterate the previous findings on this system and its individual components.

On Pt(111), formic acid adsorbs molecularly at 130 K in the strongly hydrogen-bonded α -polymorphic state.^{7,36} At lower adsorption temperatures, formic acid exists on the surface as isolated monomers or dimers that form the β -polymorph phase at higher coverage.³⁵ Above 170 K, only a bridged formate species is found with C_{2v} symmetry.^{7,34,35} Decomposition of formate occurs via dehydrogenation to CO₂ and H₂ at 260 K.⁷ Minor amounts of CO and water have also been detected.⁴

Decomposition of formic acid has been studied on single crystal CeO₂(111)²⁸ and CeO₂(100)²⁸ surfaces, on thin stoichiometric CeO₂(111) films, and on partially reduced CeO_x(111) deposited on Ru(0001).^{15,24} Adsorption of formic acid at 90 K yields formates coadsorbed with molecular formic acid. Above 200 K only formate species remain on the surfaces. Decomposition of formate yields CO₂, CO, H₂O, and H₂ on CeO₂(111)¹⁵ and, predominantly, CO and H₂ on CeO_x(111). Gordon et al.²⁴ reported tilting of the formate adsorbed in a bridging configuration, resulting in lower symmetry of the species above 400 K.

Analysis of the desorption products suggests that the reaction of formic acid on ceria cannot be described in terms of pure dehydrogenation or dehydration. Gordon et al.²⁴ concluded that the initial interaction of formic acid with ceria causes reduction of the oxide (accompanied by desorption of H₂O) and is followed by reoxidation (accompanied by desorption of CO and H₂) in a second stage. Some disagreement remains concerning the desorption temperatures of CO₂, CO, and H₂, which are substantially higher (~600 K) on single crystals CeO₂(111)²⁸ as compared to thin films.¹⁵ Formation of small amounts of formaldehyde has been detected on all samples.^{15,28}

The interaction of formic acid with supported metal/oxide systems has been studied on Au/CeO₂,⁴⁰ Pt/TiO₂,⁴¹ Pd/TiO₂,^{12,42} and Rh/Al₂O₃.⁴³ It was found that the presence of metal particles significantly modifies the decomposition pathways of formic acid. For instance, the dehydration pathway on CeO₂ was significantly attenuated in the presence of Au particles.⁴⁰

In this paper, we report a comprehensive study of formic acid adsorption and decomposition on well-ordered stoichiometric CeO₂(111), partially reduced CeO_{2-x}, and Pt/CeO₂(111) model catalysts prepared on a Cu(111) single crystal. We combine synchrotron radiation photoelectron spectroscopy (SRPES), resonant photoemission spectroscopy (RPES), and infrared reflection absorption spectroscopy (IRAS) with temperature programmed desorption (TPD). RPES turns out to be most useful in establishing the nature of the related redox interactions. In particular, the removal of lattice oxygen during water desorption, suggested by Senanayake et al.,¹⁵ could be ruled out.

2. EXPERIMENTAL METHODS

2.1. Sample Preparation. A single crystal Cu(111) disc (MaTecK GmbH, 99.999%) was used as a substrate for CeO₂(111), CeO_{2-x}, and Pt/CeO₂(111). First, Cu(111) was cleaned by several cycles of Ar⁺ sputtering (300 K, 60 min) and annealing (723 K, 5 min) until no traces of carbon or any other contaminant were found in the photoelectron spectra. Epitaxial layers of CeO₂ were prepared on clean Cu(111) by physical vapor deposition (PVD) of Ce metal (Goodfellow, 99.99%) in an oxygen atmosphere ($p_{O_2} = 5 \times 10^{-7}$ mbar, Linde, 99.999%) at 523 K, followed by annealing of the films at 523 K in an oxygen atmosphere at the same pressure for 5 min. The preparation method^{44,45} yields a continuous, stoichiometric CeO₂(111) film with a thickness in the range of 1.9–2.1 nm as determined from the attenuation of the Cu 2p_{3/2} intensity. Low energy electron diffraction (LEED) observations of the prepared films confirm the epitaxial growth of CeO₂(111) with the characteristic (1.5 × 1.5) superstructure relative to the Cu(111) substrate.⁴⁴ According to previous scanning tunneling microscopy (STM) studies, flat CeO₂(111) terraces are separated by steps and contain extended rough patches composed of small ceria particles.^{46,47} Partially reduced ceria film (CeO_{2-x}) was prepared by exposing a stoichiometric CeO₂(111) film to 45 L (Langmuir, 1 L = 1.33×10^{-6} mbar × s) of methanol by backfilling the chamber at a sample temperature of 700 K, followed by annealing at 700 K in UHV for 30 min. The procedure yields partially reduced CeO_{2-x} films, where $x = 0.16$.⁴⁸ Pt was deposited by means of PVD from a Pt wire (0.5 mm in diameter, Goodfellow, 99.99%) onto CeO₂/Cu(111) at 300 K. The nominal thickness of the deposited Pt layer was 0.4 nm as determined from the attenuation of the Cu 2p_{3/2} intensity. The structure and thermal stability of the Pt/CeO₂ systems have been discussed before.^{49,50} Briefly, Pt nanoparticles grown at 300 K preferentially nucleate at rough patches of the ceria surface. Typically, the density of Pt particles is $(5.4 \pm 1.0) \times 10^{23}$ cm⁻² and the average size of Pt particles is 3.3 ± 0.3 nm for the Pt/CeO₂ system with a nominal thickness of the Pt deposit of 0.5 nm.⁴⁹ The samples of Pt/CeO₂/Cu(111) used in SRPES and TPD studies were flash annealed to 500 K prior to formic acid exposure in order to remove potential surface impurities (such as CO) accumulated during sample preparation.

2.2. Molecular Beams and Infrared Absorption Spectroscopy (MB/IRAS). The MB/IRAS measurements were performed in an UHV apparatus at the Friedrich-Alexander-University Erlangen-Nuremberg, Germany. The setup allows exposure of the sample surface to up to four effusive beams and one supersonic beam. A beam monitor is used that permits exact MB alignment and calibration. In addition, the system is equipped with a vacuum Fourier-Transform IR (FTIR)

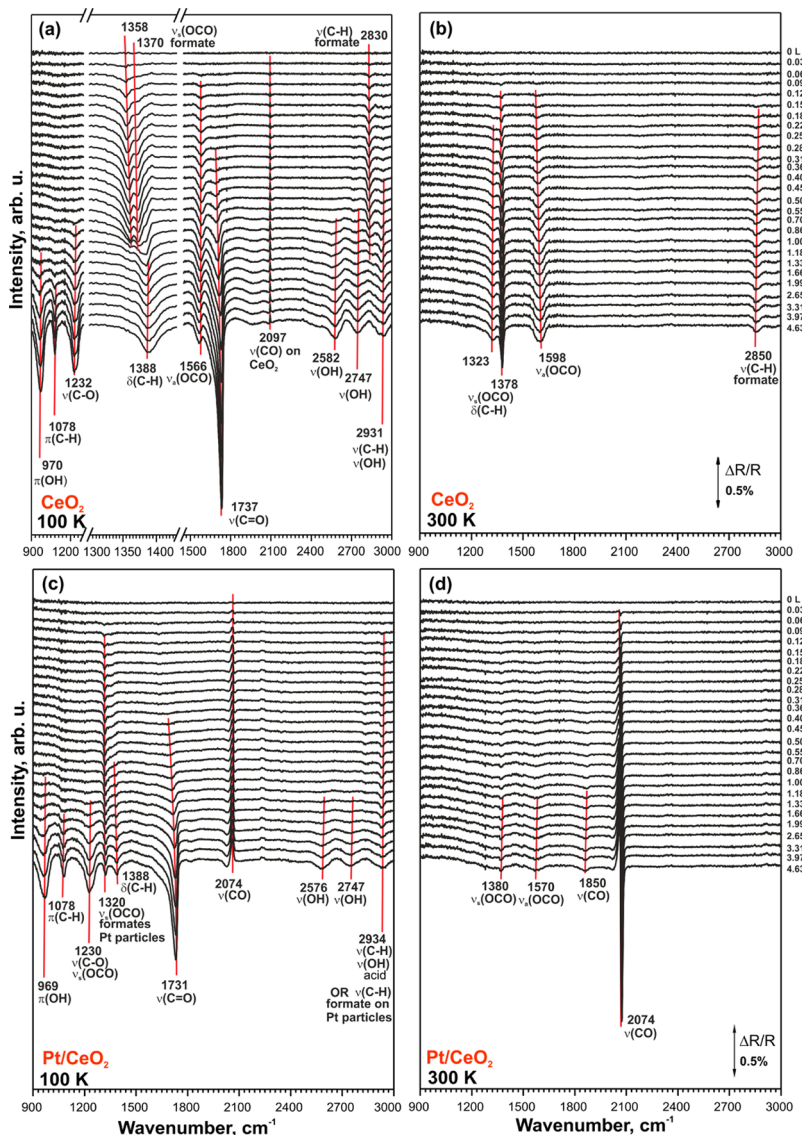


Figure 1. IRAS obtained from CeO₂(111) (a,b) and Pt/CeO₂(111) (c,d) during adsorption of HCOOH at 100 K (a,c) and 300 K (b,d).

spectrometer (Bruker IFS 66/v), two quadrupole mass spectrometers (QMS), a vacuum transfer system and a high-pressure cell.

Well-ordered CeO₂(111) and Pt/CeO₂ films on Cu(111) were prepared according to the procedures described in section 2.1. The deposition rates of Ce (1.5–2.0 nm per hour) and Pt (0.3 nm per hour) were calibrated using a quartz crystal microbalance. The resulting thickness of the CeO₂(111) film was 1.2–1.5 nm and the nominal thickness of the deposited Pt layer was 0.4 nm.

The CeO₂(111) and Pt/CeO₂(111) films were exposed to HCOOH (Acros Organics, 98–100%) at 100 and 300 K. HCOOH was dosed via an effusive beam source. The amount of HCOOH in the gas stream was calibrated by the QMS and beam monitor.

The IR spectra were acquired as follows: First, a background spectrum of the clean sample was taken. Then the sample was exposed to defined doses of HCOOH. In between each dose, an IR spectrum was recorded with a resolution of 2 cm^{-1} . The total exposures of HCOOH on the samples were 5 L at 100 and 300 K.

2.3. SRPES and RPES.

performed at the Materials Science Beamline at the Elettra synchrotron facility in Trieste, Italy. The radiation source was a bending magnet producing synchrotron light in the energy range of 21–1000 eV. The UHV end-station (base pressure 1×10^{-10} mbar) was equipped with a multichannel electron energy analyzer (Specs Phoibos 150), a rear view LEED optics, an argon sputter gun, and a gas inlet system. The basic setup of the chamber includes a dual Mg/Al X-ray source used for energy calibration of the synchrotron light and for off-line work. Additionally, two electron-beam evaporators for Ce and Pt deposition were installed.

Core level spectra of O 1s, C 1s, and Pt 4f were acquired at 650, 410, and 180 eV, respectively. The binding energies (BEs) in the spectra acquired with synchrotron radiation were calibrated with respect to the Fermi level. Additionally, Al K α radiation (1486.6 eV) was used to measure the core levels of O 1s, C 1s, Pt 4f, Ce 3d, and Cu 2p_{3/2}. All spectra were acquired at a constant pass energy and at an emission angle for the photoelectrons of 20° or 0° with respect to the sample normal, while using the X-ray source or synchrotron radiation, respectively. The total spectral resolutions achieved were 1

eV (Al $K\alpha$), 200 meV ($h\nu = 115\text{--}180\text{ eV}$), 400 meV ($h\nu = 410\text{ eV}$), and 650 meV ($h\nu = 650\text{ eV}$). The C 1s and O 1s core level spectra were fitted with a Voigt profile after subtraction of Shirley background.

VB spectra were acquired at three different photon energies ($h\nu$), 121.4, 124.8, and 115.0 eV that correspond to the resonant enhancements in Ce³⁺, Ce⁴⁺ ions, and to off-resonance conditions, respectively. Analysis of the spectra obtained with these photon energies forms the basis of RPES.⁴⁸ The Ce³⁺ resonance at a photon energy of 121.4 eV is caused by a super Coster–Kronig decay involving electron emission from Ce 4f states located about 1.4 eV below the Fermi edge. The Ce⁴⁺ resonance at a photon energy of 124.8 eV involves emission of O 2p electrons (hybridized with Ce states) from the valence band around 4.0 eV. The valence band spectrum measured at a photon energy of 115 eV is used as a background for calculation of the intensity difference between the corresponding features on- and off-resonance, denoted as the resonant enhancements for Ce³⁺ ($D(\text{Ce}^{3+})$) and for Ce⁴⁺ ($D(\text{Ce}^{4+})$). The resonant enhancement ratio (RER), calculated as $D(\text{Ce}^{3+})/D(\text{Ce}^{4+})$, is the direct measure of the change of the cerium oxidation state. All SRPES and RPES data were processed using KolXPD fitting software.⁵¹

During the experiment, the sample temperature was controlled by a DC power supply passing a current through Ta wires holding the sample. Temperatures were measured by a K-type thermocouple attached to the rear surface of the sample. Stable temperature and fast cooling after the annealing steps were achieved by simultaneous resistive heating and cooling of the manipulator with liquid nitrogen. Formic acid, HCOOH, (Acros Organics, 98–100%) was purified by five freeze–pump–thaw cycles. The investigated samples were exposed in consecutive doses to a total amount of 10 L of HCOOH at 160 K by backfilling the UHV chamber.

2.4. TPD. The TPD experiments were performed in a separate UHV system (base pressure $1 \times 10^{-10}\text{ mbar}$) at the Charles University in Prague, Czech Republic. The chamber was equipped with QMS (Pfeiffer PrismaPlus). The QMS was placed behind a differentially pumped nozzle in order to separate background contributions from molecules desorbing directly from the sample surface. The sample was heated resistively, and was attached to a liquid-nitrogen cooled cryostat, enabling the sample temperatures between 90 and 1200 K. The temperature was ramped at 2 K/s rate.

Deuterated formic acid, DCOOH, (Aldrich, 98 atomic % D, 95 wt % in water) was purified by five freeze–pump–thaw cycles. The investigated samples were exposed to a total amount of 10 L of DCOOH at 150 K.

3. RESULTS AND DISCUSSION

3.1. Adsorption Geometry of HCOOH on Stoichiometric CeO₂(111) and Pt/CeO₂(111): IRAS. IR spectra obtained from stoichiometric CeO₂(111) exposed to increasing doses of HCOOH at 100 and 300 K are displayed in Figure 1a,b, respectively. Three bands emerge in the spectra at 1358, 1566, and 2830 cm⁻¹ following adsorption of HCOOH at 100 K (Figure 1a). A small shoulder apparent at 1370 cm⁻¹ increases, while the main peak at 1358 cm⁻¹ decays with increasing dose of formic acid, producing a single sharp band at 1388 cm⁻¹. At doses higher than 0.22 L, additional bands emerge at 1700, and 2931 cm⁻¹. The band at 1700 cm⁻¹ is blue-shifted to 1737 cm⁻¹ with increasing doses of formic acid.

At highest doses, multiple bands associated with multilayer of formic acid are resolved.

In accordance with the literature,^{24,28,52,53} these are assigned to $\pi(\text{OH})$ (970 cm⁻¹), $\pi(\text{CH})$ (1078 cm⁻¹), $\nu(\text{C}-\text{O})$ (1232 cm⁻¹), $\delta(\text{C}-\text{H})$ (1388 cm⁻¹), $\nu(\text{C}=\text{O})$ (1737 cm⁻¹), $\nu(\text{OH})$ (2582, 2747 cm⁻¹), and $\nu(\text{C}-\text{H})/\nu(\text{OH})$ (2931 cm⁻¹). For a detailed discussion of the vibrational spectra of HCOOH, we refer to the literature.^{52,53} According to the locations of the $\nu(\text{C}=\text{O})$ and $\pi(\text{OH})$, the dominant structure of the multilayer formic acid is the crystalline α -polymorph.^{24,35} The absence of $\pi(\text{OH})$, $\pi(\text{CH})$ and other modes associated with molecular formic acid in the IR spectra below 1.0 L points to the presence of formate species on the surface. The corresponding formate bands are assigned to $\nu_s(\text{OCO})$ (1358, 1370 cm⁻¹), $\nu_a(\text{OCO})$ (1566 cm⁻¹), and $\nu(\text{C}-\text{H})$ (2830 cm⁻¹). Here, $\nu_s(\text{OCO})$ region contains also a contribution from the $\delta(\text{C}-\text{H})$ stretch.²⁴ The presence of $\nu(\text{C}=\text{O})$ band at 1700 cm⁻¹ and $\nu(\text{C}-\text{H})$ at 2931 cm⁻¹, unattended by the π modes below 1.0 L, may point to the presence of molecular formic acid adsorbed with its molecular plane perpendicular to the surface.²⁴ Gordon et al.²⁴ suggested that formic acid molecules have different orientation in the monolayer than in the multilayer. The remaining band at 2097 cm⁻¹ is assigned to desorption of CO, possibly originating from readsorption from the chamber background. This band was observed previously during studies of interaction of ceria-based catalysts with CO.⁵⁴

It is often stated that the $\nu_s(\text{OCO})$ region is sensitive to the structure of the formate and that the splitting between $\nu_s(\text{OCO})$ and $\nu_a(\text{OCO})$ bands may provide information on the bonding of the formate species at the surface.^{24,28,53,55} A larger separation ($\sim 300\text{ cm}^{-1}$) is often associated with monodentate species, while a smaller splitting (190–250 cm⁻¹) is typically assigned to the bidentate configuration.⁵⁶ This trend has been validated on TiO₂(110),¹⁷ ZrO₂(−111),¹⁸ and Ga₂O₃(100)¹⁹ by the DFT simulations. The assignment of the formate geometry on CeO₂, however, has been questioned by Gordon et al.²⁴ The authors reported strong sensitivity of the vibrational splitting to the presence of the coadsorbed proton and the nature of the oxygen vacancies. For instance, the increase of the vibrational splitting from 222 to 300 cm⁻¹ was predicted upon removal of the hydrogen proton from the vicinity of the bidentate formate.²⁴

In our experiment, the vibrational splitting of the formate on CeO₂ is in the range 196–275 cm⁻¹. Therefore, we assume that formates on CeO₂ would bind predominantly in the bidentate geometry. The bidentate configuration, however, was earlier ruled out for CeO₂(111) by Stubenrauch et al.²⁸ based on the O–O distance in the CeO₂(111) and bond length within the formate species. Gordon et al.,²⁴ on the other hand, argued that the bidentate coordination of the formates on CeO₂(111)/Ru(0001) in nearly C_{2v} symmetry is possible if a bridging complex is coordinated to Ce cations. As indicated by the multiple bands in the $\nu_s(\text{OCO})$ region (Figure 1a), it is likely that different structures of adsorbed formate are present on the surface. More precise identification of these structures, however, is not possible without detailed theoretical assessment.

According to Gordon et al.,²⁴ the deprotonation of formic acid to formate is complete at 250 K. Adsorption of formic acid on CeO₂(111) at 300 K (see Figure 1b) results in three bands assigned above to formate species: $\nu_s(\text{OCO})$ (1378 cm⁻¹), $\nu_a(\text{OCO})$ (1598 cm⁻¹), and $\nu(\text{C}-\text{H})$ (2850 cm⁻¹). These bands dominate the spectra throughout the whole range of

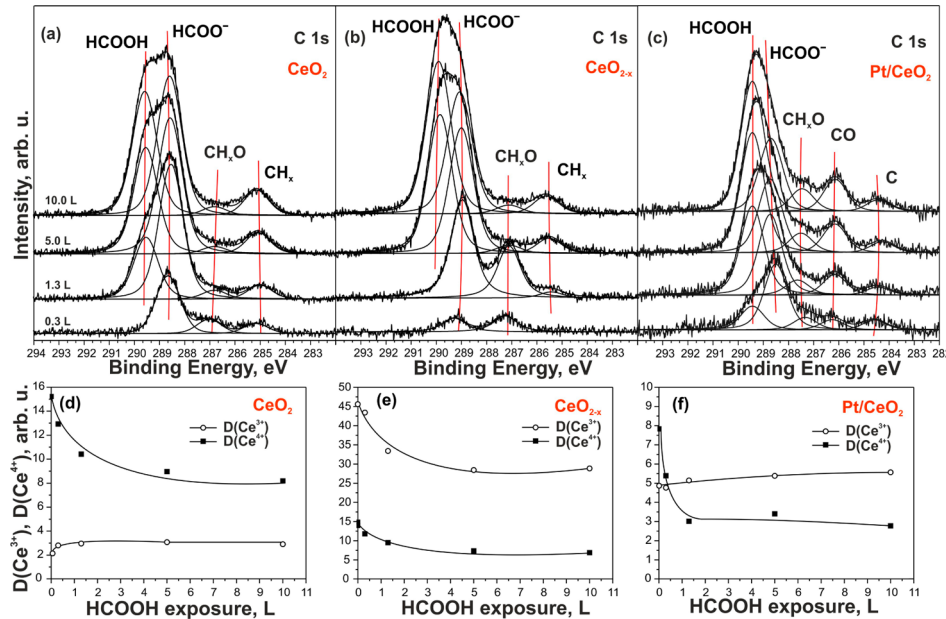


Figure 2. C 1s spectra (a–c) and evolutions of $D(Ce^{3+})$ and $D(Ce^{4+})$ (d–f) obtained from CeO₂(111) (a), CeO_{2-x} (b), and Pt/CeO₂(111) (c) during adsorption of HCOOH at 160 K.

exposures. Additionally, a small $\nu_s(OCO)$ band emerges at 1323 cm⁻¹. Earlier Siokou and Nix⁵⁷ assigned $\nu_s(OCO)$ and $\nu_a(OCO)$ bands at 1300 and 1616 cm⁻¹, respectively, to the monodentate formate formed upon interaction of the methoxy species with ceria surfaces. The presence of methoxy moieties will be discussed in section 3.2. It is likely, however, that the larger splitting in the formate formed during adsorption at 300 K (275 cm⁻¹) as compared to 150 K (196–208 cm⁻¹) may be associated with desorption of water as discussed by Gordon et al.²⁴

Next, we consider the influence of Pt on the adsorption behavior of formic acid on CeO₂. The corresponding spectra obtained from 0.4 nm Pt supported on CeO₂(111) following HCOOH exposure at 100 and 300 K are shown in Figure 1c,d, respectively.

During the first stages of HCOOH adsorption at 100 K, bands develop at 1320, 2065–2074, 2833, and 2934 cm⁻¹. At higher exposures, multiple bands associated with multilayers of formic acid emerge: $\pi(OH)$ (969 cm⁻¹), $\pi(CH)$ (1078 cm⁻¹), $\nu(C-O)$ (1230 cm⁻¹), $\delta(C-H)$ (1388 cm⁻¹), $\nu(C=O)$ (1731 cm⁻¹), $\nu(OH)$ (2576, 2747 cm⁻¹), and $\nu(C-H)/\nu(OH)$ (2934 cm⁻¹). Note that the band at 2934 cm⁻¹ is more pronounced and is different in shape during the initial stages of adsorption as compared to the 2931 cm⁻¹ band on the bare CeO₂. Therefore, it may have multiple origins. The band at 1320 cm⁻¹ has a shoulder at around 1340 cm⁻¹. Based on the observations of Ohtani et al.³⁶ and Avery et al.,⁷ we assign the bands in the low exposure region to the vibrational modes of formates on Pt as follows: $\nu_s(OCO)$ (1320 cm⁻¹), $\delta(C-H)$ (1338 cm⁻¹), and $\nu(C-H)$ (2935 cm⁻¹). The latter contains the contribution from the $\nu(C-H)$ stretch of formic acid, as indicated by the pronounced broadening of this band at higher exposures.

Importantly, the bands associated with formate on CeO₂ appear only as weak features on the Pt/CeO₂ at 1358/1370, 1566 cm⁻¹, and 2833 cm⁻¹. This observation allows us to conclude that the formic acid mainly deprotonates on Pt particles, where most of the formates are located.

Surprisingly, the band at 1566 cm⁻¹ is absent in the multilayer coverage on Pt/CeO₂. This may suggest a change in adsorption geometry of the formic acid molecules induced by the presence of Pt.

The band at 2065–2074 cm⁻¹ does not appear on the Pt-free samples. This band is assigned to $\nu(CO)$ and originates from CO adsorbed on-top of Pt particles edges and steps.⁵⁴ The S-shaped band is due to displacement of CO molecules adsorbed either from the background of the chamber or from dissociation of formate species. The $\nu(CO)$ (2065–2074 cm⁻¹) along with the band $\nu(CO)$ (1850 cm⁻¹) associated with CO adsorbed in bridging geometry⁵⁴ dominate the spectra obtained from Pt/CeO₂ following the adsorption of formic acid at 300 K (see Figure 1d). The remaining weak bands at 1380 and 1570 cm⁻¹ are assigned to the $\nu_s(OCO)$ and the $\nu_a(OCO)$ of formates on ceria. Importantly, the bands associated with formates are much weaker as compared to the bare ceria sample at 300 K (see Figure 1b). At the same time, the CO band on Pt is much more intense than that on the Pt/CeO₂ at 100 K (see Figure 1c). Thus we conclude that the formates dissociate on Pt at this temperature leaving CO adsorbed on the Pt nanoparticles. Note that CO does not adsorb on ceria at this temperature. The absence of the bands associated with formate on Pt is in good agreement with earlier studies of Avery⁷ and Columbia et al.³⁵ who reported complete formate decomposition on Pt(111) at 260 K. However, only decomposition via dehydrogenation was suggested. This pathway would not produce any CO, but exclusively CO₂ and H₂. Note that CO₂ does not adsorb on Pt at this temperature.⁵⁸ Formation of carbonates on the ceria support can also be ruled out based on the C 1s spectra obtained from Pt/CeO₂ at 300 K (the C 1s peak related to carbonates is expected at 290 eV¹⁵ and is not present in the C 1s spectra (see section 3.4).

3.2. Adsorption of HCOOH on Stoichiometric CeO₂(111), Partially Reduced CeO_{2-x}, and Pt/CeO₂(111): SRPES. C 1s spectra obtained from stoichiometric CeO₂(111)/Cu(111), CeO_{2-x}/Cu(111), and Pt/CeO₂(111) films exposed to increasing doses of HCOOH at 160 K are

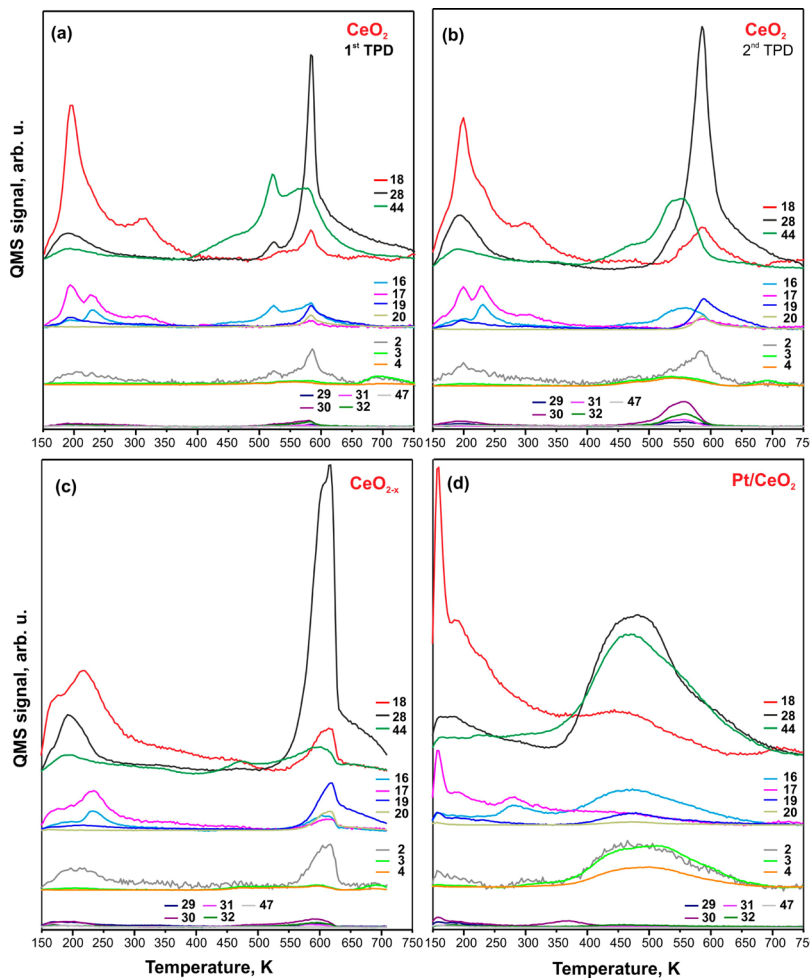


Figure 3. TPD spectra from $\text{CeO}_2(111)$ (a,b), CeO_{2-x} (c), and $\text{Pt}/\text{CeO}_2(111)$ (d) following exposure to 10 L of DCOOH at 150 K. On $\text{CeO}_2(111)$, first (a) and second (b) TPD runs are shown. All spectra are displayed on the same intensity scale. The spectra are grouped according to their intensity and offset for clarity.

shown in Figure 2a,b,c, respectively. According to Senanayake and Mullins,¹⁵ the dominant species on both $\text{CeO}_2(111)$ and CeO_{2-x} surfaces are formate (HCOO^-) and molecular formic acid.

The corresponding peaks emerge at 288.6 and 289.6 eV on CeO_2 and at 288.9 and 289.9 eV on partially reduced CeO_{2-x} . Since we did not observe any significant attenuation of formate signal during adsorption of formic acid, we assume that formate and molecular formic acid form a mixed layer on $\text{CeO}_2(111)$ and CeO_{2-x} surfaces. Additionally, we detected two types of minority species emerging at 285.0 and 287.0 eV on CeO_2 , and 285.2 and 287.2 eV on CeO_{2-x} . Considering the development of the corresponding peaks with increasing dose of formic acid on both $\text{CeO}_2(111)$ and CeO_{2-x} surfaces, we deduce that the species at 285.0–285.2 eV are decomposition products of the species at 287.0–287.2 eV. With regard to their binding energies, the species at 287.0–287.2 eV could be assigned to an alkoxy moiety, e.g., CH_3O^- gives rise to a C 1s component at 287.2 eV on ceria.⁵⁹ The feature at 285.0–285.2 eV can be assigned to either alkyl species or a partially dissociated alkyl moiety, e.g., CH_x , probably bonded to a Ce cation.⁶⁰

C 1s spectra obtained from $\text{Pt}/\text{CeO}_2(111)$ (Figure 2c) contain five components located at 289.4, 288.7, 287.5, 286.1, and 284.4 eV. The peaks at 289.4 and 288.7 eV represent contributions from molecular formic acid and formate,

respectively. Note that it is not possible to distinguish between the species adsorbed on $\text{CeO}_2(111)$ and Pt particles by SRPES. However, IRAS analysis suggests (see section 3.1) that a major fraction of the formate species is located on Pt particles. The peak at 286.1 eV is assigned to CO on Pt particles.^{61,62} The peak at 287.5 eV is again associated with methoxy species either on CeO_2 ⁵⁹ or Pt particles.⁶² Note that the CH_x species at 285.0–285.2 eV is absent on Pt/CeO_2 . Instead, the feature at 284.4 eV emerges. It is assigned to carbon on CeO_2 ⁶² or Pt particles.⁶³

The origin of the adsorbed CO on Pt particles is not clear. As mentioned in the Introduction, formic acid on Pt decomposes to CO_2 and H_2 which subsequently desorbs without dissociation to CO. It is therefore likely that the CO adsorbed on Pt/CeO_2 , at least in part, originates from dissociation of formic acid at the chamber walls.

The evolution of the resonant enhancements, $D(\text{Ce}^{3+})$ and $D(\text{Ce}^{4+})$, corresponding to the concentration of Ce^{3+} and Ce^{4+} ions on the surfaces of $\text{CeO}_2(111)$, CeO_{2-x} and $\text{Pt}/\text{CeO}_2(111)$ is plotted in Figure 2d,e,f, respectively. The formic acid adsorption causes a decrease of $D(\text{Ce}^{4+})$ on all samples. Since we do not observe a simultaneous increase in $D(\text{Ce}^{3+})$, we assume that the decrease of $D(\text{Ce}^{4+})$ primarily originates from attenuation of Ce^{4+} by adsorbed species. Similarly, on the

partially reduced CeO_{2-x} , we observe a significant decrease of $D(\text{Ce}^{3+})$ as a result of Ce^{3+} attenuation.

3.3. Decomposition of Formic Acid on Stoichiometric $\text{CeO}_2(111)$, Partially Reduced CeO_{2-x} , and Pt/ $\text{CeO}_2(111)$:

TPD. Selected TPD spectra from $\text{CeO}_2(111)/\text{Cu}(111)$, $\text{CeO}_{2-x}/\text{Cu}(111)$, and Pt/ $\text{CeO}_2(111)$ exposed to a total dose of 10 L of DCOOH at 150 K are shown in Figure 3a–d. On each sample two, subsequent TPD runs have been performed. In Figure 3, the first (a) and the second (b) TPD runs are shown only for the $\text{CeO}_2(111)$ sample. Mass spectroscopic intensities were recorded at numerous m/z ratios to account for desorption of hydrogen, CO, CO_2 , water, methane, methanol, formaldehyde, and molecular formic acid. Table 1 shows the

Table 1. The Correspondence of m/z Ratios with Detected Molecular Fragments

m/z	fragments
2	H_2
3	HD
4	D_2
14	CH_2, CD
16	$\text{CH}_4, \text{CD}_2, \text{O}$
17	$\text{OH}, \text{CHD}_2, \text{CH}_3\text{D}$
18	$\text{H}_2\text{O}, \text{OD}, \text{CH}_2\text{D}_2$
19	HDO, CHD_3
20	$\text{D}_2\text{O}, \text{CD}_4$
28	CO
29	CHO
30	$\text{CH}_2\text{O}, \text{CDO}$
31	$\text{CH}_3\text{O}, \text{CHDO}$
32	$\text{CH}_3\text{OH}, \text{CH}_2\text{DO}, \text{CD}_2\text{O}, \text{O}_2$
44	CO_2
47	DCOOH

correspondence of the m/z ratios with detected molecular fragments. The desorption products were identified with the help of the NIST mass spectra database.⁶⁴ Gas specific sensitivity factors were taken into account before comparing relative contributions of different molecules.

Decomposition of DCOOH on CeO_2 and CeO_{2-x} proceeds in two distinct temperature ranges. In the low temperature range (below 400 K), the dominant products are water (H_2O , HDO), hydrogen (H_2), CO, and CO_2 . On CeO_2 (see Figures 3a and 3b), water desorbs yielding two distinct peaks at 195 K (H_2O , HDO) and 314 K (H_2O). It should be noted that the H_2O desorption peak at 195 K may contain a large contribution from water condensed on the samples from the background as well as from the residual water in the DCOOH supply. Desorption of physisorbed water from $\text{CeO}_2(111)$ is usually found below 200 K.⁶⁵ Analysis of the fragmentation patterns suggests that also some D_1 -methane (CH_3D) desorbs at temperatures around 230 K. Note that mass 16 originates from the CH_2D fragment, while mass 17 contains contributions from CH_3D and the OH cracking fragment of water. Desorption of CH_2D_2 at the same temperature cannot be completely ruled out. Taking into account fragmentation patterns of water and methane, CH_4 and D_2O were ruled out. Hydrogen (H_2) desorbs in a broad peak centered around 205 K. CO₂ and CO desorb simultaneously at 192 K with an intensity ratio 0.3.

The high temperature range (above 400 K) is dominated by CO and CO₂ desorption. CO₂ desorbs in a broad peak with three maxima at 465, 522, and 575 K. CO desorbs in a narrow

interval peaking around at 585 K. The ratio of CO₂ to CO produced above 400 K is ~0.8 in first and 0.4 in second TPD runs. Small amounts of H₂ desorb at 525, 560, and 586 K. Surprisingly, neither HD nor D₂ was detected, except for small amount of HD desorbing above 650 K. Instead, small signals from masses 16, 17, 18, 19, and 20 appear at 586 K. The masses 18, 19, and 20 originate from desorption of water: H₂O, HDO, and D₂O, respectively. The masses 16 and 17 occur with simultaneous desorption of CO₂ and H₂O, respectively, and represent cracking fragments of these products. Desorption of formaldehyde (CD₂O or CHDO) from stoichiometric $\text{CeO}_2(111)$ was observed only in the second TPD run. Note that annealing of stoichiometric CeO₂ to 750 K in the first TPD run resulted in a slight reduction of the surface (see Section 3.4).⁵⁰ Apparently, slightly reduced ceria possesses specific reaction sites for formaldehyde production. In a related system, Idriss et al.²⁹ identified such sites on fully oxidized [114]-faceted TiO₂(001) as low-coordinated Ti⁴⁺ cations. Senanayake and Mullins¹⁵ also observed traces of formaldehyde on stoichiometric CeO₂ films deposited on Ru(0001) at 700 K. Evidently, the production of formaldehyde competes with desorption of CO₂. As a result, the sharp CO₂ desorption peak is missing in the second TPD run at 522 K, which is the onset temperature for formaldehyde desorption.

On CeO_{2-x} (see Figure 3c), water (H₂O) desorbs in two peaks at 175 and 220 K with a long tail extending to 500 K. The desorption peak of water at 314 K observed on CeO₂ is not present on CeO_{2-x} (compare panels a and c in Figure 3). Methane (CH₃D) desorbs at 210 K. The amount of water desorbed from both CeO_{2-x} and CeO₂ in low temperature region is comparable, whereas about 2 times higher amount of CO desorbs from CeO_{2-x} . The ratio between CO₂ (183 K) and CO (186 K) is close to 0.25. The main difference between the two samples is the absence of mass 19 (HDO) on CeO_{2-x} below 400 K. Instead, mass 30 is present, indicating trace desorption of formaldehyde (CD₂O or CHDO) at 178 K.

Considerable differences between CeO₂ and CeO_{2-x} were detected in the high temperature region. In particular, the total amount of CO₂ desorbing from CeO_{2-x} is much smaller (about 23%), with a CO₂ to CO ratio of ~0.11. A broad CO₂ spectrum has at least three maxima at 470, 588, and 613 K. CO desorbs in a narrow region with two maxima at 605 and 622 K. Hydrogen (H₂) and masses 16, 17, 18, 19, and 20 appear with maxima at two temperatures, 600 and 621 K. They are closely related to CO desorption. Similarly to CeO₂, the corresponding products originate from desorption of water (D₂O, H₂O, and HDO).

Same as on CeO₂, desorption of D₂ and HD from CeO_{2-x} is minor. Desorption of formaldehyde (CD₂O or CHDO) occurs at 586 K. However, the amount of formaldehyde desorbing from CeO_{2-x} is much smaller as compared to the second TPD run from slightly reduced CeO₂. Once again, this observation demonstrates that the presence of specific sites rather than oxygen vacancies is responsible for the formaldehyde production on ceria.

It must be noted that the TPD spectra obtained from CeO₂(111) and CeO_{2-x} (Figures 3a,c) are only in partial agreement with those obtained by Senanayake and Mullins¹⁵ from CeO₂(111)/Ru(0001) and CeO_{2-x}/Ru(0001). The major differences concern desorption temperatures of the observed products. The reason for this disagreement is not clear. The common finding of our study and the work of Senanayake and Mullins¹⁵ is the lack of molecular hydrogen in the TPD spectra

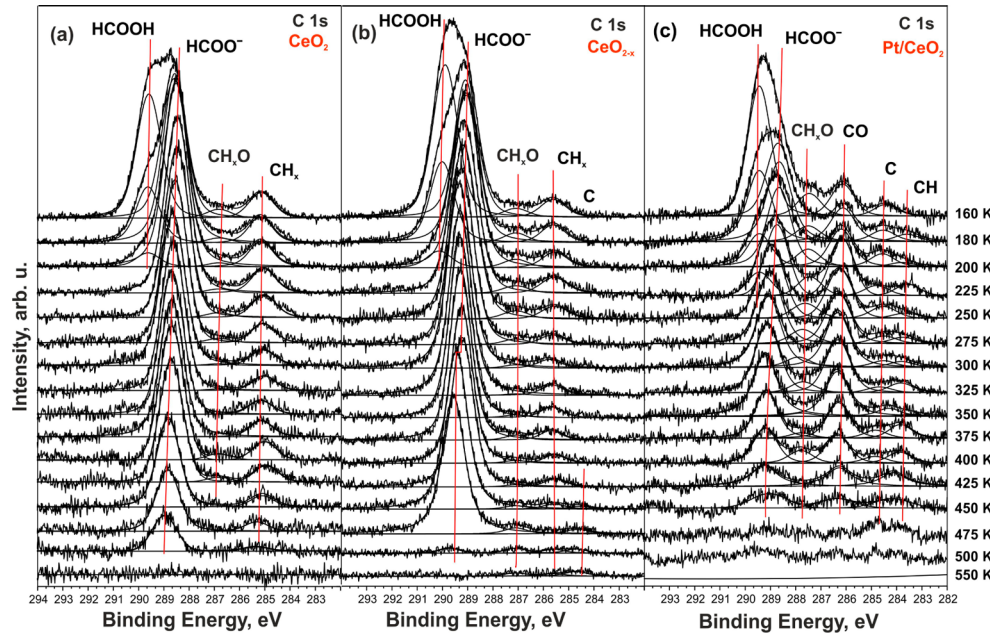


Figure 4. C 1s spectra obtained during annealing of $\text{CeO}_2(111)$ (a), CeO_{2-x} (b), and $\text{Pt}/\text{CeO}_2(111)$ (c) exposed to 10 L of HCOOH at 160 K.

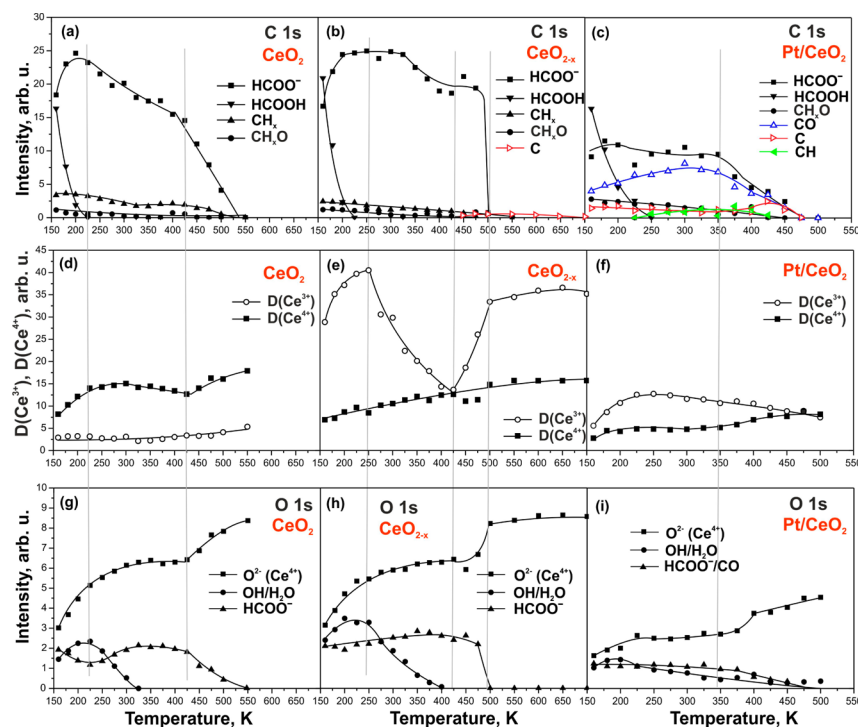


Figure 5. Integrated intensities of C 1s (a–c) and O 1s (g–i) spectral components and resonant enhancements, $D(\text{Ce}^{3+})$ and $D(\text{Ce}^{4+})$ (d–f), as a function of temperature on CeO_2 (a,d,g), CeO_{2-x} (b,e,h), and Pt/CeO_2 (c,f,i).

from CeO_2 . Formation of methane could, at least in part, explain this anomaly. Desorption of methane (CH_3D) points to withdrawal of hydrogen released during deprotonation of molecular formic acid upon adsorption or annealing of the adsorbate. Previously, formation of either methanol or methane has been registered during decomposition of formic acid on ceria-based catalysts.^{40,66} In our experiment, we exclude methanol formation because we did not observe any larger cracking fragments. For instance, for methanol, mass 16 (CH_2D) should be accompanied by mass 32 (CH_2DO , major fragment) that was absent. Desorption of methane and water

from CeO_2 and CeO_{2-x} means that hydroxyl groups do not participate in the decomposition of formate above 400 K.

On Pt/CeO_2 (see Figure 3d), the TPD spectra differ substantially from those observed on CeO_2 and CeO_{2-x} . Here, considerable amounts of water desorb between 150 and 650 K with maxima at 160 K (H_2O , HDO), 189 K (H_2O), 230 K (H_2O), and 460 K (H_2O). Methane (CH_3D) desorbed at 280 K, and is followed by desorption of H_2 at 305 K. Small amounts of hydrogen desorb also at 160 K. In the low temperature region, similarly to the CeO_2 and CeO_{2-x} cases, CO_2 and CO desorption occurs at about 170 K, with the ratio of 0.5. Both,

CO and CO₂ are the major desorption products at higher temperature with two indistinct maxima: 470 and 560 K, 475 and 590 K, respectively, and broad shoulders around 600 K. Taking into account that only 50% of CO desorbing from Pt/CeO₂ comes from the decomposition of formic acid on the surface (see Section 3.4), the CO₂/CO ratio amounts to 1.4. In sharp contrast to CeO₂ and CeO_{2-x}, a considerable amount of hydrogen (H₂, D₂, HD) desorbs above 350 K in parallel with CO₂, with two maxima at 470 and 560 K. Desorption of CO is also accompanied by desorption of water (H₂O, HDO, and D₂O) around 460 K. Desorption of formaldehyde from Pt/CeO₂ occurs in small amounts below 200 K and between 300 and 400 K.

3.4. Decomposition of Formic Acid on Stoichiometric CeO₂(111), Partially Reduced CeO_{2-x}, and Pt/CeO₂(111): SRPES. C 1s spectra obtained during stepwise annealing of stoichiometric CeO₂(111), partially reduced CeO_{2-x}, and Pt/CeO₂(111) exposed to HCOOH at 160 K are shown in Figure 4a,b,c, respectively. The species formed on the samples have been discussed in section 3.2. Briefly, formate (288.6–288.9 eV) and molecularly adsorbed formic acid (289.4–289.9 eV) are the majority species on all samples. Methoxy (287.0–287.5 eV) on ceria, CH_x (285.0–285.2 eV) coordinated to Ce cations, and CO (286.1 eV) and C (284.4 eV) on ceria or Pt particles are the minority species. The thermal evolution of the C 1s (a–c) and O 1s (g–i) intensities of the surface species along with the evolution of the resonant enhancements, D(Ce³⁺) and D(Ce⁴⁺), (d–f) on CeO₂, CeO_{2-x}, and Pt/CeO₂(111) are shown in Figure 5. The O 1s spectra (not shown) have been fitted assuming contributions from the lattice oxygen, O²⁻(Ce⁴⁺) (529.3–529.7 eV),⁶⁷ OH/H₂O (531.0–532.0 eV),⁶⁷ HCOO⁻ (532.0–532.2 eV),¹⁵ and HCOOH (533.8 eV).

We observe that molecular formic acid desorbs or decomposes below 250 K, triggering the increase of formate and water on all samples (see Figure 5a,g). Since we do not observe any significant signal from molecular formic acid in TPD spectra of the studied samples (see section 3.3), we conclude that HCOOH decomposes to formate and water, hydrogen, CO, CO₂, and methane. Most likely, the decomposition of HCOOH below 250 K proceeds via a bimolecular mechanism on both CeO₂ and CeO_{2-x} and does not involve net redox processes on the ceria substrate. Most importantly, lattice oxygen is *not* removed from ceria upon desorption of water below 400 K. The development of D(Ce³⁺) and D(Ce⁴⁺) between 160 and 250 K supports this claim (see Figure 5d). The increase observed in both D(Ce⁴⁺) and D(Ce³⁺) on CeO₂ and CeO_{2-x}, respectively (see Figures 5d,e) is accompanied by the increase of O 1s signal from the lattice oxygen in ceria, O²⁻(Ce⁴⁺) (see Figures 5g,h) and therefore is caused by the recovery of the signal from attenuation by the adsorbate. Note that D(Ce⁴⁺) and D(Ce³⁺) were selectively attenuated during adsorption of formic acid on CeO₂ and CeO_{2-x}, respectively.

The presence of methoxy and CH_x species on the surface of both CeO₂ and CeO_{2-x} (see Figure 4a,b) is most likely connected to desorption of methane in the low temperature region and desorption of formaldehyde in the high temperature region (see section 3.3). Hydrogenation of oxygenates in the presence of an excess of atomic hydrogen on oxide surfaces has been reported earlier.⁶⁸

Continuous desorption/decomposition of formate on CeO₂ above 250 K is accompanied by a gradual shift of the

corresponding C 1s peak from 288.6 to 289.0 eV (see Figure 4a). The development of D(Ce⁴⁺) and D(Ce³⁺) indicates that CeO₂ is not involved as a redox partner in the decomposition: the increase of D(Ce⁴⁺) occurs simultaneously with the increase of the O²⁻(Ce⁴⁺) signal (compare panels d and g of Figure 5). However, a slight increase of RER, calculated as D(Ce³⁺)/D(Ce⁴⁺), from 0.14 before adsorption of formic acid to 0.3 indicates a loss of a small portion of lattice oxygen upon annealing of the adsorbate to 700 K. Such a small reduction of ceria is caused by annealing rather than interaction with formic acid.

On CeO_{2-x} formate is stable up to 325 K (see Figure 5b) while the corresponding C 1s peak gradually shifts from 288.9 to 289.2 eV (see Figure 4b). An abrupt shift from 289.2 to 289.6 occurs between 425 and 450 K, followed by the fast decomposition of formate at 500 K. In sharp contrast to CeO₂, the decomposition of formate on CeO_{2-x} results in a dramatic decrease of the D(Ce³⁺) resonance (see Figure 5e) between 250 and 425 K. The drop of the D(Ce³⁺) intensity might be related to a change of the formate adsorption geometry. Gordon et al.²⁴ reported occurrence of multiple low symmetry formate species on partially reduced ceria between 250 and 400 K. The authors considered insertion of one of the formate oxygen atoms into oxygen vacancy. This would lead to partial attenuation of Ce³⁺ signal. However, the large D(Ce³⁺) decrease suggests partial reoxidation of topmost layer of ceria. A possible explanation could be a redistribution of Ce³⁺ cations triggered by the completion of the coordination sphere of cerium. We assume that Ce³⁺ may diffuse (i.e., by electron transfer) into deeper ceria layers that are not accessible with RPES due to its high surface sensitivity.

According to TPD (see section 3.3), the majority of the species desorbing from CeO_{2-x} above 500 K are CO, water, and hydrogen. A small decrease of RER from its initial value determined before adsorption (2.77) to 2.24 suggests partial reoxidation of ceria. This may result either from side production of H₂ during dehydration of formate or from partial dissociation⁴⁸ of CO₂ formed via dehydrogenation, which is the minor reaction channel on CeO_{2-x}.

On Pt/CeO₂, formate species adsorbed on CeO₂ and Pt cannot be distinguished. A slow decrease of the corresponding C 1s intensity at 288.7 eV coincides with the increase of the CO contribution at 286.1 eV upon annealing to 350 K (see Figures 4c and 5c). Above 350 K, CO desorption and decomposition of formate species proceed in parallel. Note, that most of the CO accumulated upon adsorption does not originate from the decomposition of formic acid (see section 3.2). However, the following increase of CO upon annealing is attributed to the decomposition of adsorbed species on the surface. The quantity of CO formed on the surface upon annealing corresponds only to 50% of the total amount of CO present on Pt particles (compare corresponding C 1s intensities at 160 and 300 K, Figure 5c). Small amounts of carbon located at 284.4 eV, and, probably, CH⁶⁹ at 283.7 eV, are deposited above 350 K and removed by annealing of the sample to 500 K. During the annealing of Pt/CeO₂, D(Ce⁴⁺) increases due to recovery from attenuation by adsorbed species. However, the development of D(Ce³⁺) on Pt/CeO₂ is very distinct from that on CeO₂ and CeO_{2-x} (compare panel f to panels d and e in Figure 5).

Reduction of ceria occurs upon annealing of Pt/CeO₂ to 250 K. Note that the increase of D(Ce³⁺) is not connected to attenuation of Ce³⁺ ions, since only Ce⁴⁺ ions were attenuated

during adsorption at 160 K (see Figure 2f). The reduction of ceria in the low temperature region can be explained by a spillover of hydrogen from Pt particles to ceria.⁷⁰ Formate decomposes into CO₂ and H₂ at 260 K on Pt(111).^{7,35} CO₂ desorbs at 260 K while hydrogen remains on Pt(111) until 300 K.³⁵ Earlier we demonstrated that the spillover of hydrogen from Pt to ceria on Pt/CeO₂ takes place below 200 K and is followed by the reverse spillover of hydrogen from ceria to Pt above 260 K.⁷⁰ Reverse hydrogen spillover and desorption of H₂ lead to reoxidation of ceria so that the initial D(Ce³⁺)/D(Ce⁴⁺) ratio is recovered at 310 K.⁷⁰ In strong contrast to this, reoxidation of ceria proceeds very slowly and is not complete at 500 K. For comparison, RERs before adsorption of formic acid and after annealing to 500 K are 0.63 and 0.91, respectively. The observed behavior points to a partial reduction of the ceria support. This effect may have two possible origins: (1) spillover of hydrogen and its recombination with formate on the ceria support or (2) side production of H₂O during decomposition of formate via dehydrogenation. The first interpretation is in line with the suggestion of Benitez et al.,⁴³ who proposed recombination of formate back to formic acid on lanthanide-promoted alumina and its following migration to supported Rh particles. The second interpretation is, however, more plausible because we did not detect any molecular formic acid in the TPD spectra from Pt/CeO₂. The enhanced CO₂/CO ratio on Pt/CeO₂ points to preferential dehydrogenation of formate, which is in line with the high yield of molecular hydrogen discussed in section 3.3. However, a small fraction of hydrogen likely recombines with lattice oxygen on ceria and desorbs in the form of water (see Figure 3d), leading to net reduction of the support. Note that hydroxyl groups are present on Pt/CeO₂ up to 500 K (see Figure 5i). Significant suppression of CO formation has also been observed on Au/CeO₂.⁴⁰

CONCLUSIONS

Adsorption and decomposition of formic acid on CeO₂(111), CeO_{2-x}, and Pt/CeO₂ has been studied by means of SRPES, RPES, IRAS, and TPD. We have found that adsorption of formic acid at 100–160 K yields formate species and molecular formic acid coadsorbed on CeO₂, CeO_{2-x}, and Pt/CeO₂. On Pt/CeO₂, formate species are predominantly located on Pt particles. Adsorption of formic acid at 300 K yields formate on CeO₂ and CeO_{2-x} and CO on Pt. On CeO₂, formate was found in both bidentate (100 and 300 K) and monodentate (300 K) configurations.

The decomposition of formic acid proceeds in two distinct temperature intervals. In the low temperature region (below 400 K) desorption of CO, CO₂, H₂, and H₂O occurs most likely via a bimolecular decomposition mechanism. Additionally, methane has been detected at 210 K (CeO_{2-x}), 230 K (CeO₂), and 280 K (Pt/CeO₂). Desorption of methane causes removal of hydrogen deposited on the surface during dehydrogenation of formic acid. In the high-temperature region (above 400 K), desorption of CO, CO₂, H₂, and H₂O strongly depends on the stoichiometry of ceria and presence of Pt particles. Desorption of CO₂ is suppressed on partially reduced CeO_{2-x} but is enhanced on Pt/CeO₂. Traces of formaldehyde have been found on all samples. However, on stoichiometric CeO₂(111), formaldehyde is formed only in the second TPD run, after annealing the film to 750 K (when the oxide is slightly understoichiometric).

The RPES study shows that reaction of formic acid on stoichiometric CeO₂(111) has no influence on the oxidation state of cerium cations. This result suggests that lattice oxygen is *not removed* upon desorption of water as suggested earlier.¹⁵ This assumption holds also for desorption of water from partially reduced CeO_{2-x}. On the contrary, reaction of formic acid on CeO_{2-x} results in significant reoxidation of ceria between 250 and 400 K due to an electron transfer from Ce³⁺ to formate. The latter is followed by the rapid decomposition of formate and reduction of ceria. On Pt/CeO₂(111), hydrogen spillover from Pt to the support occurs below 260 K. Unlike on the Pt-free samples, reverse hydrogen spillover from ceria to Pt results in desorption of molecular hydrogen from Pt/CeO₂ above 350 K.

Overall, reaction of formic acid on CeO_{2-x} and Pt/CeO₂ results in partial net reoxidation and net-reduction of ceria, respectively. This is likely caused by minor side production of H₂ during formate dehydration on CeO_{2-x} and H₂O during formate dehydrogenation on Pt/CeO₂.

AUTHOR INFORMATION

Corresponding Author

*E-mail: Yaroslava.Lykhach@chemie.uni-erlangen.de; Fax: +49 9131 8528867; Tel: +49 9131 8528867.

Author Contributions

The manuscript was written through contributions of all authors. All authors have given approval to the final version of the manuscript.

Notes

The authors declare no competing financial interest.

ACKNOWLEDGMENTS

The authors gratefully acknowledge financial support by the Deutsche Forschungsgemeinschaft (DFG) and by the Ministry of Education of the Czech Republic (LG12003 and LD11047). We acknowledge additional support from the DFG within the excellence cluster “Engineering of Advanced Materials” in the framework of the Excellence Initiative as well as support from the COST Action CM1104 “Reducible oxide chemistry, structure and functions”. M.H. gratefully acknowledges support by a grant of the “Fonds der Chemischen Industrie”. Travel support by the DAAD (project 50755695) is gratefully acknowledged. F.D. acknowledges support by GACR 202/09/H041 and GAUK 610112. F.D. and V.J. acknowledge support by GAČR 204/11/1183. Y.L., V.J., N.T., and K.C.P. thank Elettra for excellent working conditions and support.

ABBREVIATIONS

SRPES, synchrotron radiation photoelectron spectroscopy; RPES, resonant photoelectron spectroscopy; IRAS, infrared reflection absorption spectroscopy; MB, molecular beams; FTIR, Fourier-Transform IR; TPD, temperature programmed desorption; QMS, quadrupole mass spectrometer; LEED, low energy electron diffraction; STM, scanning tunneling microscopy; UHV, ultrahigh vacuum; RER, resonant enhancement ratio

REFERENCES

- (1) Bridgwater, A. V. Production of High Grade Fuels and Chemicals from Catalytic Pyrolysis of Biomass. *Catal. Today* **1996**, *29* (1–4), 285–295.

- (2) Güell, B. M.; van Rossum, G.; van Swaaij, W. P. M.; Kersten, S. R. A.; Lefferts, L.; Seshan, K. Challenges in the Production of Sustainable Fuels from Pyrolysis Oil - Design of Efficient Catalyst for Gasification of Char. *Appl. Catal., B* **2011**, *101* (3–4), 587–597.
- (3) Columbia, M. R.; Thiel, P. A. The Interaction of Formic Acid with Transition Metal Surfaces, Studied in Ultrahigh Vacuum. *J. Electroanal. Chem.* **1994**, *369*, 1–14.
- (4) Abbas, N.; Madix, R. J. Surface Reaction Modification: The Effect of Structured Overlayers of Sulfur on the Kinetics and Mechanism of the Decomposition of Formic Acid on Pt(111). *Appl. Surf. Sci.* **1983**, *16*, 424–440.
- (5) Chtaib, M.; Delrue, J. P.; Caudano, R. Decomposition of HCOOH on Gold Studied by XPS and TDS Spectroscopies and Its Behaviour Under Very Low Energy Electron Excitation. *Phys. Scr.* **1983**, *T4*, 133–137.
- (6) Iglesia, E.; Boudart, M. Unimolecular and Bimolecular Formic Acid Decomposition on Copper. *J. Phys. Chem.* **1986**, *90*, 5212–5274.
- (7) Avery, N. R. Adsorption of Formic Acid on Clean and Oxygen Covered Pt(111). *Appl. Surf. Sci.* **1982**, *11/12*, 774–783.
- (8) Bowker, M.; Madix, R. J. XPS, UPS, and TDS Studies of the Reaction of Formaldehyde and Formic Acid with the Cu(110) Surface. *Surf. Sci.* **1981**, *102*, 542–565.
- (9) Hu, C. Q.; Ting, S. W.; Chan, K. Y.; Huang, W. Reaction Pathways Derived from DFT for Understanding Catalytic Decomposition of Formic Acid into Hydrogen on Noble Metals. *Int. J. Hydrogen Energy* **2012**, *37* (21), 15956–15965.
- (10) Zheng, T.; Stacchiola, D.; Saldin, D. K.; James, J.; Sholl, D. S.; Tysoe, W. T. The Structure of Formate Species on Pd(111) Calculated by Density Functional Theory and Determined Using Low Energy Electron Diffraction. *Surf. Sci.* **2005**, *574* (2–3), 166–174.
- (11) Trillo, J. M.; Munuera, G.; Criado, J. M. Catalytic Decomposition of Formic Acid on Metal Oxides. *Catal. Rev.* **1972**, *7* (1), 51–86.
- (12) Bowker, M.; Stone, P.; Bennett, R.; Perkins, N. Formic Acid Adsorption and Decomposition on TiO₂(110) and on Pd/TiO₂(110) Model Catalysts. *Surf. Sci. Rep.* **2002**, *511*, 435–448.
- (13) Gercher, V. A.; Cox, D. F. Formic Acid Decomposition on SnO₂(110). *Surf. Sci.* **1994**, *312*, 106–114.
- (14) Chong, S. V.; Idriss, H. The Reaction of Carboxylic Acid on UO₂(111). Effect of Gas-Phase Acidity and Surface Defects. *Surf. Sci.* **2002**, *504*, 145–158.
- (15) Senanayake, S. D.; Mullins, D. R. Redox Pathways for HCOOH Decomposition over CeO₂ Surfaces. *J. Phys. Chem. C* **2008**, *112* (26), 9744–9752.
- (16) Dilara, P. A.; Vohs, J. M.; HREELS, T. P. D. Investigation of the Reaction of Formic Acid on Zirconium Dioxide (100). *J. Phys. Chem.* **1993**, *97* (49), 12919–12923.
- (17) Rotzinger, F. P.; Kesselman-Truttmann, J. M.; Hug, S. J.; Shklover, V.; Gratzel, M. Structure and Vibrational Spectrum of Formate and Acetate Adsorbed from Aqueous Solution onto the TiO₂ Rutile (110) Surface. *J. Phys. Chem. B* **2004**, *108* (16), 5004–5017.
- (18) Korhonen, S. T.; Calatayud, M.; Krause, A. O. I. Structure and Stability of Formates and Carbonates on Monoclinic Zirconia: A Combined Study by Density Functional Theory and Infrared Spectroscopy. *J. Phys. Chem. C* **2008**, *112* (41), 16096–16102.
- (19) Calatayud, M.; Collins, S. E.; Baltanas, M. A.; Bonivardi, A. L. Stability of Formate Species on β -Ga₂O₃. *Phys. Chem. Chem. Phys.* **2009**, *11* (9), 1397–1405.
- (20) Bandara, A.; Kubota, J.; Wada, A.; Domen, K.; Hirose, C. Adsorption and Reactions of Formic Acid on (2 × 2)-NiO(111)/Ni(111) Surface. 2. IRAS Study under Catalytic Steady-State Conditions. *J. Phys. Chem. B* **1997**, *101*, 361–368.
- (21) Bandara, A.; Kubota, J.; Wada, A.; Domen, K.; Hirose, C. Adsorption and Decomposition of Formic Acid on the NiO(111)-p(2 × 2) Surface: TPD and Steady State Kinetics Studies. *Surf. Sci.* **1996**, *364*, L580–L586.
- (22) Borowiak, M. A.; Jamróz, M. H.; Larsson, R. Catalytic Decomposition of Formic Acid on Oxide Catalysts - An Impulse-Oscillation Model Approach to the Unimolecular Mechanism. *J. Mol. Catal. A: Chem.* **1999**, *139*, 97–104.
- (23) Borowiak, M. A.; Jamróz, M. H.; Larsson, R. Catalytic Decomposition of Formic Acid on Oxide Catalysts III. IOM Model Approach to Bimolecular Mechanism. *J. Mol. Catal. A: Chem.* **2000**, *152*, 121–132.
- (24) Gordon, W. O.; Xu, Y.; Mullins, D. R.; Overbury, S. H. Temperature Evolution of Structure and Bonding of Formic Acid and Formate on Fully Oxidized and Highly Reduced CeO₂(111). *Phys. Chem. Chem. Phys.* **2009**, *11*, 11171–11183.
- (25) Vayssilov, G. N.; Mihaylov, M.; Petkov, P. S.; Hadjiivanov, K. I.; Neyman, K. M. Reassignment of the Vibrational Spectra of Carbonates, Formates, and Related Surface Species on Ceria: A Combined Density Functional and Infrared Spectroscopy Investigation. *J. Phys. Chem. C* **2011**, *115* (47), 23435–23454.
- (26) Falconer, J. L.; Madix, R. J. The Kinetics and Mechanism of the Autocatalytic Decomposition of HCOOH on Clean Ni(110). *Surf. Sci.* **1974**, *46*, 473–504.
- (27) Madix, R. J.; Falconer, J. L. Surface Stabilized Reaction Intermediate: Formic Anhydride. *Surf. Sci.* **1975**, *51*, 546–548.
- (28) Stubenrauch, J.; Broska, E.; Vohs, J. M. Reaction of Carboxylic Acids on CeO₂(111) and CeO₂(100). *Catal. Today* **1996**, *28*, 431–441.
- (29) Idriss, H.; Lusvardi, V. S.; Barreau, M. A. Two Routes to Formaldehyde from Formic Acid on TiO₂(001) Surfaces. *Surf. Sci.* **1996**, *348*, 39–48.
- (30) Tanner, R. E.; Sasahara, A.; Liang, Y.; Altman, E. I.; Onishi, H. Formic Acid Adsorption on Anatase TiO₂(001)-(1 × 4) Thin Films Studied by NC-AFM and STM. *J. Phys. Chem. B* **2002**, *106*, 8211–8222.
- (31) Xu, C.; Goodman, D. W. Structure Sensitivity of Oxide Surfaces: The Adsorption and Reaction of Carbon Monoxide and Formic Acid on NiO(100) and NiO(111). *Catal. Today* **1996**, *28*, 297–303.
- (32) Matsumoto, T.; Bandara, A.; Kubota, J.; Hirose, C.; Domen, K. Adsorption and Reaction of Formic Acid on a (2 × 2) NiO(111)/Ni(111) Surface. 3. IRAS Studies on the Characterization of Reaction Sites Using CO and the Behavior of Surface Hydroxyl Species. *J. Phys. Chem. B* **1998**, *102*, 2979–2984.
- (33) Miura, T.; Kobayashi, H.; Domen, K. Density Functional Study of Formate Decomposition on NiO(111) Surface. *J. Phys. Chem. B* **2001**, *105*, 10001–10006.
- (34) Luo, Q.; Feng, G.; Beller, M.; Jiao, H. Formic Acid Dehydrogenation on Ni(111) and Comparison with Pd(111), and Pt(111). *J. Phys. Chem. C* **2012**, *116*, 4149–4156.
- (35) Columbia, M. R.; Crabtree, A. M.; Thiel, P. A. The Temperature and Coverage Dependences of Adsorbed Formic Acid and Its Conversion to Formate on Pt(111). *J. Am. Chem. Soc.* **1992**, *114*, 1231–1237.
- (36) Ohtani, T.; Kubota, J.; Wada, A.; Kondo, J. N.; Domen, K.; Hirose, C. IRAS and TPD Study of Adsorbed Formic Acid on Pt(110)-(1 × 2) Surface. *Surf. Sci.* **1996**, *368*, 270–274.
- (37) Solymosi, F.; Kiss, J.; Kovács, I. Adsorption of HCOOH on Rh(111) and Its Reaction with PreadSORBED Oxygen. *Surf. Sci.* **1987**, *192*, 47–65.
- (38) Hayden, B. E.; Prince, K.; Woodruff, D. P.; Bradshaw, A. M. An IRAS Study of Formic Acid and Surface Formate Adsorbed on Cu(110). *Surf. Sci.* **1983**, *133*, 589–604.
- (39) Youngs, T. G. A.; Haq, S.; Bowker, M. Formic Acid Adsorption and Oxidation on Cu(110). *Surf. Sci.* **2008**, *602*, 1775–1782.
- (40) Gazsi, A.; Bánsági, T.; Solymosi, F. Decomposition and Reforming of Formic Acid on Supported Au Catalysts: Production of CO-Free H₂. *J. Phys. Chem. C* **2011**, *115*, 15459–15466.
- (41) Raskó, J.; Kecskés, T.; Kiss, J. Formaldehyde Formation in the Interaction of HCOOH with Pt/TiO₂. *J. Catal.* **2004**, *224*, 261–268.
- (42) Chang, Z.; Thornton, G. Effect of Pd on the Interaction of Formic Acid with TiO₂(111). *Surf. Sci.* **2000**, *459*, 303–309.
- (43) Benítez, J. J.; Carrizosa, I.; Odriozola, J. A. Mass Spectrometry and In Situ Infrared Diffuse Reflectance Analysis of the Decomposition

- of HCOOH Adsorbed on Ln_2O_3 -promoted Rh/ Al_2O_3 catalysts. *J. Chem. Soc. Faraday Trans.* **1993**, *89* (17), 3307–3312.
- (44) Šutara, F.; Cabala, M.; Sedláček, L.; Skála, T.; Škoda, M.; Matolín, V.; Prince, K. C.; Cháb, V. Epitaxial Growth of Continuous $\text{CeO}_2(111)$ Ultra-Thin Films on $\text{Cu}(111)$. *Thin Solid Films* **2008**, *516* (18), 6120–6124.
- (45) Matolín, V.; Libra, J.; Matolínová, I.; Nehasil, V.; Sedláček, L.; Šutara, F. Growth of Ultra-Thin Cerium Oxide Layers on $\text{Cu}(111)$. *Appl. Surf. Sci.* **2007**, *254* (1), 153–155.
- (46) Staudt, T.; Lykhach, Y.; Hammer, L.; Schneider, M. A.; Matolín, V.; Libuda, J. A Route to Continuous Ultra-Thin Cerium Oxide Films on $\text{Cu}(111)$. *Surf. Sci.* **2009**, *603* (23), 3382–3388.
- (47) Dvořák, F.; Stetsovych, O.; Steger, M.; Cherradi, E.; Matolínová, I.; Tsud, N.; Škoda, M.; Skála, T.; Mysliveček, J.; Matolín, V. Adjusting Morphology and Surface Reduction of $\text{CeO}_2(111)$ Thin Films on $\text{Cu}(111)$. *J. Phys. Chem. C* **2011**, *115*, 7496.
- (48) Staudt, T.; Lykhach, Y.; Tsud, N.; Skála, T.; Prince, K. C.; Matolín, V.; Libuda, J. Ceria Reoxidation by CO_2 : A Model Study. *J. Catal.* **2010**, *275*, 181.
- (49) Lykhach, Y.; Staudt, T.; Lorenz, M. P. A.; Streber, R.; Bayer, A.; Steinrück, H. P.; Libuda, J. Microscopic Insights into Methane Activation and Related Processes on Pt/Ceria Model Catalysts. *ChemPhysChem* **2010**, *11* (7), 1496–1504.
- (50) Vayssilov, G. N.; Lykhach, Y.; Migani, A.; Staudt, T.; Petrova, G. P.; Tsud, N.; Skála, T.; Bruix, A.; Illas, F.; Prince, K. C.; et al. Support Nanostructure Boosts Oxygen Transfer to Catalytically Active Platinum Nanoparticles. *Nat. Mater.* **2011**, *10*, 310–315.
- (51) <http://www.kolibrik.net/science/kolkpd/>.
- (52) Millikan, R. C.; Pitzer, K. S. The Infrared Spectra of Dimeric and Crystalline Formic Acid. *J. Am. Chem. Soc.* **1958**, *80*, 3515–3521.
- (53) Sim, W. S.; Gardner, P.; King, D. A. Multiple Bonding Configurations of Adsorbed Formate on $\text{Ag}\{111\}$. *J. Phys. Chem.* **1996**, *100*, 12509–12516.
- (54) Happel, M.; Mysliveček, J.; Johánek, V.; Dvořák, F.; Stetsovych, O.; Lykhach, Y.; Matolín, V.; Libuda, J. Adsorption Sites, Metal Support Interactions, and Oxygen Spillover Identified by Vibrational Spectroscopy of Adsorbed CO: A Reference Study on Pt/Ceria Model Catalysts. *J. Catal.* **2012**, *289*, 118–126.
- (55) Li, C.; Domen, K.; Maruya, K.; Onishi, T. Spectroscopic Identification of Adsorbed Species Derived from Adsorption and Decomposition of Formic-Acid, Methanol, and Formaldehyde on Cerium Oxide. *J. Catal.* **1990**, *125* (2), 445–455.
- (56) Busca, G.; Lorenzelli, V. Infrared Spectroscopic Identification of Species Arising from Reactive Adsorption of Carbon Oxides on Metal-Oxide Surfaces. *Mater. Chem.* **1982**, *7* (1), 89–126.
- (57) Siokou, A.; Nix, R. M. Interaction of Methanol with Well-Defined Ceria Surfaces: Reflection/Absorption Infrared Spectroscopy, X-ray Photoelectron Spectroscopy, and Temperature-Programmed Desorption Study. *J. Phys. Chem. B* **1999**, *103* (33), 6984–6997.
- (58) Kao, C. L.; Carlsson, A.; Madix, R. J. The Adsorption Dynamics of Molecular Carbon Dioxide on Pt(111) and Pd(111). *Surf. Sci.* **2002**, *497* (1–3), 356–372.
- (59) Mullins, D. R.; Robbins, M. D.; Zhou, J. Adsorption and Reaction of Methanol on Thin-Film Cerium Oxide. *Surf. Sci.* **2006**, *600* (7), 1547–1558.
- (60) Senanayake, S. D.; Gordon, W. O.; Overbury, S. H.; Mullins, D. R. Adsorption and Reaction of Acetone over $\text{CeOx}(111)$ Thin Films. *J. Phys. Chem. C* **2009**, *113* (15), 6208–6214.
- (61) Wang, J. G.; Li, W. X.; Borg, M.; Gustafson, J.; Mikkelsen, A.; Pedersen, T. M.; Lundgren, E.; Weissenrieder, J.; Klikovits, J.; Schmid, M.; et al. One-Dimensional PtO_2 at Pt Steps: Formation and Reaction with CO. *Phys. Rev. Lett.* **2005**, *95* (25), 2561021–2561024.
- (62) Matolínová, I.; Johánek, V.; Mysliveček, J.; Prince, K. C.; Skála, T.; Škoda, M.; Tsud, N.; Vorokhta, M.; Matolín, V. CO and Methanol Adsorption on (2×1) Pt(110) and Ion-Eroded Pt(111) Model Catalysts. *Surf. Interface Anal.* **2011**, *43*, 1325–1331.
- (63) Lykhach, Y.; Staudt, T.; Tsud, N.; Skála, T.; Prince, K. C.; Matolín, V.; Libuda, J. Enhanced Reactivity of Pt Nanoparticles Supported on Ceria Thin Films During Ethylene Dehydrogenation. *Phys. Chem. Chem. Phys.* **2011**, *13*, 253–261.
- (64) Stein, S. E., *Mass Spectra*; National Institute of Standards and Technology: Gaithersburg, MD, <http://webbook.nist.gov> (retrieved August 11, 2012).
- (65) Matolín, V.; Matolínová, I.; Dvořák, F.; Johánek, V.; Mysliveček, J.; Prince, K. C.; Skála, T.; Stetsovych, O.; Tsud, N.; Václavů, M.; et al. Water Interaction with $\text{CeO}_2(111)/\text{Cu}(111)$ Model Catalyst Surface. *Catal. Today* **2012**, *181* (1), 124–132.
- (66) Diagne, C.; Idriss, H.; Pepin, I.; Hindermann, J. P.; Kiennemann, A. Temperature-Programmed Desorption Studies on Pd/ CeO_2 after Methanol and Formic Acid Adsorption and Carbon Monoxide-Hydrogen Reaction. *Appl. Catal.* **1989**, *50*, 43–53.
- (67) Lykhach, Y.; Johánek, V.; Alexandrov, H.; Kozlov, S. M.; Happel, M.; Skála, T.; Petkov, P. S.; Tsud, N.; Vayssilov, G. N.; Prince, K. C.; et al. Water Chemistry on Model Ceria and Pt/Ceria Catalysts. *J. Phys. Chem. C* **2012**, *116* (22), 12103–12113.
- (68) Chen, B.; Falconer, J. L. Hydrogenation of Organic Oxygenates on $\text{Ni}/\text{Al}_2\text{O}_3$ and Ni/SiO_2 . *J. Catal.* **1994**, *147*, 72–81.
- (69) Fuhrmann, T.; Kinne, M.; Tränkenschuh, B.; Papp, C.; Zhu, J. F.; Denecke, R.; Steinrück, H.-P. Activated Adsorption of Methane on Pt(111) — An In Situ XPS Study. *New J. Phys.* **2005**, *7* (107), 1–19.
- (70) Lykhach, Y.; Staudt, T.; Vorokhta, M.; Skála, T.; Johánek, V.; Prince, K. C.; Matolín, V.; Libuda, J. Hydrogen Spillover Monitored by Resonant Photoemission Spectroscopy. *J. Catal.* **2012**, *285*, 6–9.